Journal of Hazardous Materials 436 (2022) 129251

Contents lists available at ScienceDirect

Journal of Hazardous Materials

journal homepage: www.elsevier.com/locate/jhazmat

Environmental application of chlorine-doped graphitic carbon nitride: Continuous solar-driven photocatalytic production of hydrogen peroxide

Mengqiao Li [a,1], Qinmin Zheng [a,1], David P. Durkin [b], Hanning Chen [c,*], Danmeng Shuai [a,*,2]

[a] Department of Civil and Environmental Engineering, The George Washington University, Washington, DC 20052 USA
[b] Department of Chemistry, United States Naval Academy, Annapolis, MD 21402 USA
[c] Department of Chemistry, American University, Washington, DC 20016 USA

HIGHLIGHTS

- Cl-doped g-C_3N_4 was synthesized via a solvothermal method.
- Cl dopant decreased the g-C_3N_4 bandgap and promoted charge transfer.
- Cl dopant lowered the activation energy of the rate-determining step in H_2O_2 formation.
- In the presence of isopropanol H_2O_2 was continuously produced on Cl-doped g-C_3N_4.

GRAPHICAL ABSTRACT

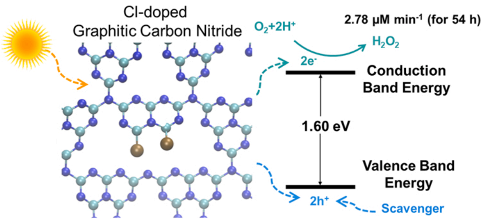

ARTICLE INFO

Editor: Meiping Tong

Keywords:
Graphitic carbon nitride
Sustainable production of H_2O_2
Doping
Metal-free photocatalysts

ABSTRACT

Solar-driven photocatalytic generation of H_2O_2 over metal-free catalysts is a sustainable approach for value-added chemical production. Here, we synthesized chlorine-doped graphitic carbon nitride (Cl-doped g-C_3N_4) through a solvothermal method to effectively produce H_2O_2 with a rate of 1.19 ± 0.06 μM min^{-1} under visible light irradiation, which was improved by 104 times compared to pristine g-C_3N_4. Continuous net production of H_2O_2 was realized at a rate of 2.78 ± 0.10 μM min^{-1} up to 54 h with isopropanol as the hole scavenger, whereas H_2O_2 production was only sustained for ~ 6 h without scavengers. Both molecular simulations and advanced spectroscopic characterizations elucidated that the Cl dopant increased the charge transfer rate, decreased the bandgap, and reduced the activation energy of the rate-limiting step of O_2 reduction, all of which favored H_2O_2 production. This work implemented a novel metal-free photocatalyst for sustainable H_2O_2 production and elucidated the mechanism for promoting H_2O_2 production that can guide future photoreactive nanomaterial design.

1. Introduction

Hydrogen peroxide (H_2O_2), a liquid compound widely used as bleach and an oxidant, is considered one of the 100 most important chemical compounds (Myers, 2007). It has broad environmental applications such as odor elimination, pollution control, water purification, disinfection, and many others (Myers, 2007; Campos-Martin et al., 2006; Melchionna et al., 2019). The global market size of H_2O_2 was 1.44 billion dollars in 2020 even though various industries were negatively impacted by the COVID-19 pandemic, and the rising demand for H_2O_2 from the

---

* Corresponding authors.
E-mail addresses: hchen@american.edu (H. Chen), danmengshuai@gwu.edu (D. Shuai).

[1] Equal contribution

[2] Website: http://materwatersus.weebly.com/

https://doi.org/10.1016/j.jhazmat.2022.129251
Received 4 April 2022; Received in revised form 11 May 2022; Accepted 25 May 2022
Available online 30 May 2022
0304-3894/

healthcare industry is fueling the market growth at an annual rate of 5.7% from 2020 to 2028 (Grand View Research, 2021). Ever since the 1940 s, the large-scale production of H_2O_2 has been almost exclusively relying on the anthraquinone autooxidation process (Campos-Martin et al., 2006). During the process, an anthraquinone is reduced by H_2 to the corresponding hydroquinone in the presence of catalysts, then the hydroquinone is autoxidized back to the anthraquinone in the presence of O_2 and produces H_2O_2. Although H_2O_2 can be efficiently synthesized during the reaction cycles, the processes of solution regeneration, impurities removal, and H_2O_2 extraction requires significant energy and chemical input, which is unsustainable. In addition, chemicals and solvents used for the anthraquinone autooxidation process are considered as hazardous materials. Thus, there is a pressing need in developing simpler and greener protocols for H_2O_2 production, especially for on-site H_2O_2 production based on the needs. Solar-driven photocatalysis has thus been explored as a promising approach for H_2O_2 generation since it can potentially utilize solar energy, water, and oxygen gas as the only energy and chemical input to improve the sustainability of chemical synthesis (Fukuzumi et al., 2018).

Photocatalytic H_2O_2 production over metal-containing semiconductors, such as TiO_2, ZnO, CdS, $BiVO_4$, and WO_3, has been widely studied (Baran et al., 2019; Hirakawa et al., 2016; Kim et al., 2016; Nosaka and Y. Nosaka, 2017; Shiraishi et al., 2013). For example, Kim et al. deposited Au nanoislands of various sizes on TiO_2 films to accelerate electron-hole separation (Kim et al., 2019). Although H_2O_2 was efficiently generated under ultraviolet (UV) light irradiation, the produced H_2O_2 suffered from UV light induced decomposition. Moreover, UV light only makes up roughly 4% of solar terrestrial radiation and thus solar energy cannot be effectively utilized by pristine TiO_2 (Li et al., 2016). According to the simulation of Goliaei et al., TiO_2 supported Ag_2Au_2 clusters were predicted to be good candidates for adsorbing visible and infrared light to generate H_2O_2 (Goliaei and Seriani, 2019). However, noble metals were needed and the decomposition of H_2O_2 on the surface of metals was commonly observed (Shiraishi et al., 2014a; Wei et al., 2018a).

Recently, graphitic carbon nitride (g-C_3N_4) has emerged as a promising photocatalyst for broad chemical, biomedical, and environmental applications due to its visible-light responsibility, low cost, superior stability, and high biocompatibility (Ong et al., 2016; Zheng et al., 2017; Zhou et al., 2021). In 2009, Wang et al. first reported the great potential of g-C_3N_4 for photocatalytic water splitting (Wang et al., 2009). Shen et al. applied g-C_3N_4 for biofilm control and realized environmental pathogen inactivation under visible light irradiation (Shen et al., 2021). Tsukamoto et al. discovered the photocatalytic activity of g-C_3N_4 for H_2O_2 generation (Shiraishi et al., 2014b). However, pristine g-C_3N_4 suffers from insufficient light absorption, poor charge transfer, and fast recombination of photoinduced electron-hole pairs, thus exhibiting only moderate photocatalytic activities. In this regard, there is an urgent need to advance the photocatalytic performance of g-C_3N_4 for H_2O_2 production (Zhu et al., 2021). Recently, heteroatom doping with metal elements, such as Na, K, Fe, and Cu, and nonmetal elements, such as S, O, P, and Cl, has been used to enhance the photocatalytic performance of g-C_3N_4 for NO removal, organic degradation, and hydrogen evolution (Li et al., 2019, 2018; Long et al., 2020; Wang et al., 2019; Xiong et al., 2018; Yang et al., 2020; Yi et al., 2020; Zhu et al., 2020). Specifically, due to its moderate electronegativity, Cl is believed to be the desired dopant in regulating the electronic structure of g-C_3N_4, promoting charge carrier utilization efficiency, and enhancing oxygen adsorption (Guo et al., 2019; Long et al., 2020).

In this work, we introduced Cl dopant into the g-C_3N_4 framework via a facile solvothermal synthesis method. Under visible light irradiation, the H_2O_2 generation rate over Cl-doped g-C_3N_4 (denoted as MCC) was 104 times higher than that of pristine g-C_3N_4 (denoted as M). The long-term photocatalytic performance of MCC was also evaluated, and the H_2O_2 generation rate remains as $2.78 \pm 0.10\ \mu M\ min^{-1}$ throughout 54 h. Integrating advanced microscopic and spectroscopic characterizations with density functional theory (DFT) simulations, we highlighted the critical role of Cl dopant on the energy band structure, charge carrier transfer, and oxygen protonation of g-C_3N_4 and elucidated how Cl doping promoted H_2O_2 production in photocatalysis. This work sheds light on developing effective metal-free photocatalysts for solar-driven H_2O_2 production. It will pave the way for on-site H_2O_2 generation and its applications of disinfection, medical care, hygiene practices, food sanitation, and water purification, especially in developing countries, remote areas, and regions after natural disasters.

2. Experimental section

2.1. Chemicals and reagents

Chemicals and reagents utilized include melamine (99%, ACROS organics), cyanuric chloride (99%, ACROS organics), 0.1 N H_2SO_4 (Sigma-Aldrich), *N,N*-diethyl-1,4-phenylenediammonium sulfate (DPD, 98%, Sigma-Aldrich), peroxidase from horseradish (POD, lyophilized powder, ~150 U mg^{-1}, Sigma-Aldrich), hydrogen peroxide (30% in water, Sigma-Aldrich), sodium sulfate (>99%, Sigma-Aldrich), phosphoric acid (85% in water), potassium phosphate monobasic (≥99%, Fisher scientific), potassium phosphate dibasic anhydrous (≥99%, Fisher scientific), ethanol (99.5%, Sigma-Aldrich), sodium hydroxide (≥98%, Sigma-Aldrich), boric acid (≥99.5%, Sigma-Aldrich), perfluorinated resin solution containing Nafion 1100 W (5 wt% in lower aliphatic alcohols and water, contains 15–20% water, Sigma-Aldrich), *N,N*-dimethylformamide (≥99%, Sigma-Aldrich), acetonitrile (Fisher scientific, HPLC grade), isopropyl alcohol (Sigma-Aldrich, HPLC grade).

All reagents were used as received without further purification.

2.2. Synthesis of g-C_3N_4

MCC, the Cl-doped g-C_3N_4, was synthesized by a solvothermal method (Cui et al., 2012). 15 mmol cyanuric chloride and 7.5 mmol melamine were put into a 100 mL of Teflon-lined autoclave and mixed with 60 mL of acetonitrile. After mixing for 12 h, the autoclave was sealed and maintained at 180 °C for 96 h and then cooled down to room temperature naturally. The obtained product was washed by acetonitrile, ultrapure water (18.2 MΩ·cm at 25 °C), and ethanol sequentially to remove impurities, and then dried at 60 °C. For comparison, M, the pristine g-C_3N_4, was synthesized via the thermal polycondensation of melamine based on the method described in our previous study (Zheng et al., 2016). Cl-removed MCC was obtained via the thermal treatment of MCC at 500 °C under N_2 protection for 1 h (Xie et al., 2016).

2.3. Characterization of g-C_3N_4

The morphological, optical, physical, and chemical properties of different g-C_3N_4 samples were characterized. Transmission electron microscopy (TEM, FEI Talos™ F200X) and scanning electron microscopy (SEM, JEOL 6700 F) were used to characterize the morphology and element distribution of the g-C_3N_4 samples. For TEM analysis, samples suspended in ethanol were dropped on 400 mesh copper grids with ultrathin carbon films supported by a lacey carbon film and dried at room temperature. High-angle annular dark-field scanning transmission electron microscopy with energy dispersive X-ray spectroscopy (HAADF-STEM-EDS) mapping was conducted under the 200 kV mode. For SEM characterization, sample suspensions were cast onto sample stubs, and SEM micrographs were collected at 10 kV by a secondary electron detector. Optical absorption spectra of the g-C_3N_4 samples were recorded by a Varian Cary 500 Scan UV/Vis system. Specifically, the optical bandgaps of the g-C_3N_4 samples were evaluated from the Kubelka-Munk equation and the Tauc plot (Li et al., 2021; Tauc et al., 1966; Zheng et al., 2016).

$$\frac{K}{S} = \frac{(1-R)^2}{2R} = F(R); \quad (1)$$

where K, S, and R refer to the absorption coefficient, the specular reflectance, and the diffuse reflectance, respectively, and $F(R)$ is the Kubelka-Munk function. Assuming the scattering coefficient remains as a constant and $F(R)$ is proportional to the absorption coefficient, the Tauc relation is:

$$y = [F(R)h\nu]^n = A\left(h\nu - E_g\right); \quad (2)$$

where h and υ refer to the Planck constant (6.63×10^{-34} J s) and the photon frequency, respectively. A is the proportionality constant, and n is ½ since the g-C_3N_4 is an indirect bandgap semiconductor. By plotting the curve of y versus $h\upsilon$ and extrapolating the linear portion of y to $y = 0$, the bandgaps of g-C_3N_4 samples were determined.

Surface functional groups of the g-C_3N_4 samples were determined by attenuated total reflectance-Fourier transform infrared spectroscopy (ATR-FTIR, iSO10 Nicolet Thermo), from 4000 to 525 cm^{-1} with a resolution of 4 (0.421 cm^{-1} data spacing). The bonding environment and surface elemental composition of the g-C_3N_4 samples were characterized by X-ray photoelectron spectroscopy (XPS). A PHI 5400 system with an Mg Kα source (1253.6 eV) was used for analysis under ultrahigh vacuum conditions (pressure $<10^{-8}$ Torr). Ejected photoelectrons were measured with a hemispherical energy analyzer operated at 58.7 eV constant pass-energy. Peak positions were referenced to C1s (284.5 eV), and CasaXPS was used to determine the chemical composition and atomic concentrations at the surface (up to ca. 10 nm).

Electrochemical measurements were conducted in a three-electrode system equipped with a Gamry Potentiostat to evaluate the charge transfer resistance of the g-C_3N_4 samples. An indium tin oxide (ITO) glass coated with samples, Pt wire, and Ag/AgCl KCl (3 M) were used as the working, counter, and reference electrodes, respectively, and 0.5 M Na_2SO_4 solution (pH 6.43) was used as the electrolyte. The ITO glasses were cleaned by sonication in acetone, ultrapure water, and ethanol sequentially, and dried at room temperature. 10 mg of g-C_3N_4 samples were suspended in a mixture with 180 μL of ethanol and 20 μL of Nafion by sonication. Then the suspensions were dropped onto the pre-cleaned ITO glasses to make sure the effective area was 1 cm^2. The electrochemical impedance spectra (EIS) were collected in the dark over a frequency range of 5 mHz to 100 kHz with an amplitude of 10 mV at the zero potential (Han et al., 2019; Liang et al., 2015; Wei et al., 2018b).

2.4. Determination of H_2O_2 concentration

The accumulated concentration of H_2O_2 was measured by the DPD method (Bader et al., 1988). The fresh DPD reagent and POD reagent were prepared weekly by dissolving 0.1 g of DPD in 10 mL of 0.1 N H_2SO_4, and 10 mg of POD in 10 mL of ultrapure water, respectively. Both DPD and POD reagents were stored in the dark at 4 °C. For analysis, a 400 μL aliquot of the sample was mixed with 100 μL of 25 mM phosphate buffer (pH 6), 15 μL of the DPD reagent, and 15 μL of the POD reagent. Absorbance was measured at 551 nm (UV–vis spectrophotometer, Hach DR 6000) and the resulting H_2O_2 concentration was determined via a calibration curve generated with known concentrations of H_2O_2. The standard H_2O_2 solutions were prepared from the dilution of 30 wt% H_2O_2 solutions (Sigma-Aldrich) as the stock, and the H_2O_2 concentration in the stock was determined by measuring H_2O_2 absorbance at 240 nm and the molar absorption coefficient of 38.1 M^{-1} cm^{-1} (Goldstein et al., 2007). The detection limit of the DPD method was on the order of 10^{-7} M.

2.5. Photocatalytic H_2O_2 production

Photosynthesis of H_2O_2 was first conducted in a jacketed beaker under the irradiation of a 1000 W xenon lamp equipped with a water optical filter to remove infrared light. A long-pass optical filter ($\lambda > 400$ nm) for simulating the visible light in solar irradiation or an AM 1.5 G filter for simulating the average sunlight irradiation for the 48 contiguous U.S. states over one year was used. Outdoor experiments were also conducted at midday (11:00 am to 5:00 pm, May 9th, 2018) on the George Washington University campus, with sky conditions ranging from clear to partly cloudy and an ambient temperature of 25 °C. The artificial light source of white light emitting diodes (LEDs, 7 W) was also used for evaluating H_2O_2 production. The photon fluences and irradiances of light sources were recorded by a spectroradiometer (AvaSpec ULS2048L) and reported in Table S1. For all H_2O_2 generation tests unless specified, dissolved oxygen in the air was used as the reactant at the ambient temperature and pressure, the pH values of the experiments were controlled at 7 by using 15 mL of 1 mM phosphate buffer solutions, the photocatalyst loading was maintained at 1 g L^{-1}, and no scavenger was used. To improve the performance of H_2O_2 production, 10% (v/v) isopropanol was introduced as the hole scavenger for some tests (Su et al., 2010). To understand the impact pH on H_2O_2 production, tests were also conducted at pH 3, 7, and 9, respectively, by using a 10 mM phosphate buffer, phosphate buffer, and borate buffer, respectively. The photosynthetic reactions were conducted under magnetic stirring at 500 rpm. All experiments were performed with at least three independent replicates.

The solar-to-chemical (SCC) conversion efficiency (η) was evaluated under the irradiation of simulated sunlight (xenon lamp, AM 1.5 G) and outdoor sunlight by the following equation (Teng et al., 2021):

$$\eta \quad (\%) = \frac{\Delta G_{H_2O_2} \times n_{H_2O_2}}{t_{ir} \times S_{ir} \times I_{AM}} \times 100\%; \quad (3)$$

Where $\Delta G_{H_2O_2}$ represents the free energy for H_2O_2 formation (117 kJ mol^{-1}), $n_{H_2O_2}$ is the molar amount of generated H_2O_2 (mol) and t_{ir} is the irradiation time (s). The irradiation area (S_{ir}) is 1.26×10^{-3} m^2, and the overall irradiation intensity (I_{AM}) of the simulated AM 1.5 global spectrum and outdoor sunlight (250–700 nm) is 129 and 312 W m^{-2}, respectively (Table S1).

2.6. Computational simulation

A 6 × 6 supercell (Fig. S1) of nitrogen-bridged heptazine was adopted to model the pristine g-C_3N_4. Its structure was optimized by the density functional theory (DFT) (Hohenberg and Kohn, 1964) before its bandgap was evaluated by the same method. Unless otherwise specified, all DFT simulations in the present study were carried out by CP2K quantum mechanics software (VandeVondele et al., 2005) with Goedecker-Teter-Hutter (GTH) pseudopotential (Goedecker et al., 1996), Heyd-Scuseria-Ernzehof (HSE06) exchange-correlation functional (Krukau et al., 2006), polarized-valence-double-ζ (PVDZ) basis set (Woon and Dunning, 1994). Moreover, a generalized implicit solvation model (Bani-Hashemian et al., 2016) with a dielectric constant of 78.4 was applied to mimic the aqueous environment. Since the protonation state of the Cl-doped g-C_3N_4 and its hydrogenated derivative (after removing Cl) could be critical to O_2 binding, the first step of catalyzed H_2O_2 production, we utilized the ChemAxon package to estimate their pKa values by solving the Hammett-Taft equation (Csizmadia et al., 1997).

3. Results and Discussion

3.1. Characterization of Cl-doped g-C_3N_4

The morphology and microstructure of the g-C_3N_4 samples were investigated with HAADF-STEM (Fig. 1) and SEM (Fig. S2). Compared to the g-C_3N_4 synthesized by thermal polycondensation (M, Fig. S2 left), g-C_3N_4 synthesized by the solvothermal method (MCC, Fig. S2 right) primarily showed a nanofibrous structure. The SEM indicated that the

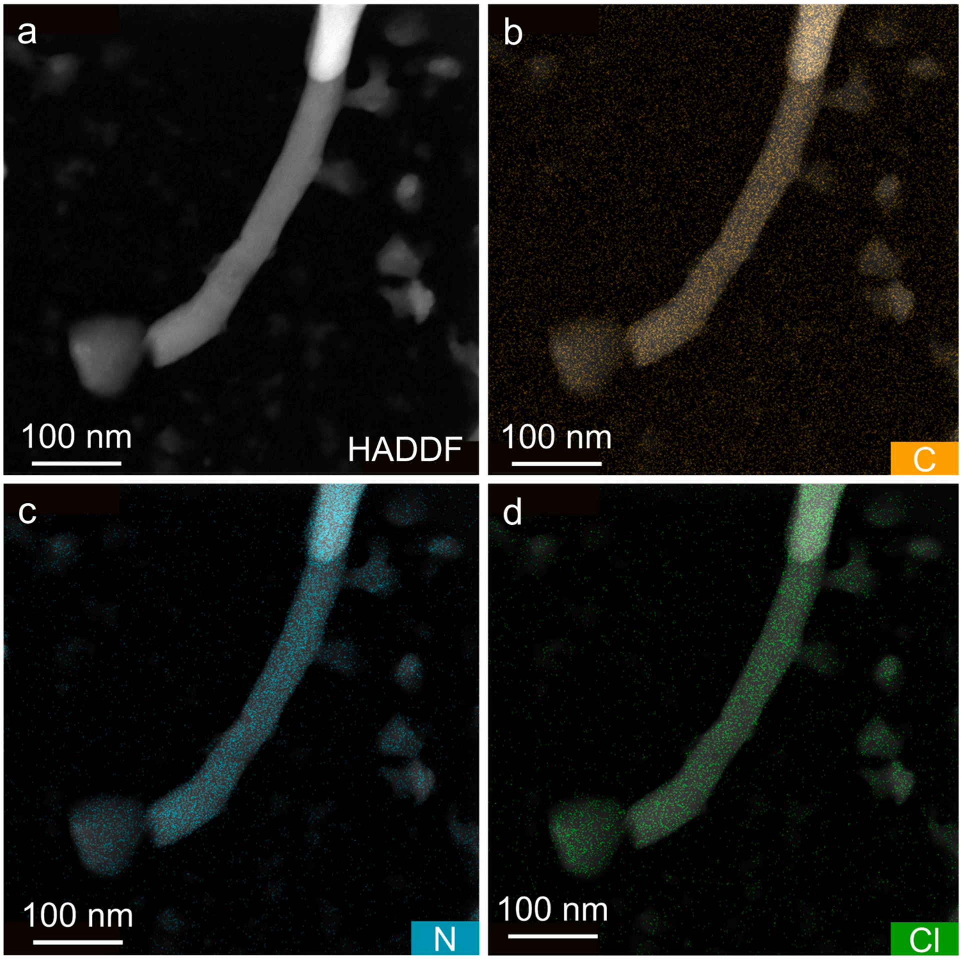

Fig. 1. (a) High-angle annular dark-field scanning transmission electron microscopy (HAADF-STEM) of Cl-doped graphitic carbon nitride (MCC) and its energy dispersive X-ray spectroscopy (EDS) mapping of (b) C, (c) N, and (d) Cl.

nanofibers had a uniform width of ~50 nm and lengths of several micrometers, which were consistent with TEM characterizations (Fig. 1a). The EDS mapping of C (Fig. 1b), N (Fig. 1c), and Cl (Fig. 1d) exhibited the homogenous distribution of Cl through MCC, and the atomic percentage of Cl was around 1.83%. Clearly, the subcritical polar solvent, i.e., acetonitrile, served as an annealing fluid and provided a sufficient thermodynamic force to polymerize melamine and cyanuric chloride molecules to form nanofibers (Cui et al., 2012). As shown in Fig. S3, XPS was used to study the surface composition and the chemical state of MCC. The deconvolution of the C 1*s* signals produced two peaks centered at 284.5 and 287.6 eV, which could be ascribed to C-C and C═N, respectively (Teng et al., 2021). In the high-resolution N 1*s* spectrum of MCC, the peaks centered at 398.2 and 399.7 eV were indexed as sp^2-hybridized aromatic nitrogen atoms (C═N-C) and tertiary nitrogen ($N\text{-}(C)_3$) groups, respectively (Shi et al., 2018). The atomic ratio of carbon to nitrogen was 1.08 (Table S2), much larger than the stoichiometry of graphitic carbon nitride with a perfect structure (0.75), and it could be explained by the loss of amine groups or the introduction of N vacancies (Liu et al., 2016). These results indicated that melamine and cyanuric acid molecules did assemble to form extended aromatic carbon-nitrogen frameworks. The atomic percentage of Cl detected by XPS was 2.4%, consistent with the EDS mapping analysis. Moreover, MCC exhibited clear Cl 2*p* signals with two pairs of Cl $2p_{3/2}$ and Cl $2p_{1/2}$ peaks at 200.0 and 201.5 eV corresponding to C-Cl species, and 196.7 and 198.4 eV for the ionic Cl species, respectively (Gu et al., 2016), which confirmed the introduction of Cl into the carbon-nitrogen framework. FTIR spectrum (Fig. S4) was also used to study the chemical structure and surface functional groups of MCC. The 776 cm^{-1} region was indexed as the breathing mode of triazine units, and the 1100–1600 cm^{-1} region was considered as the stretching vibration mode of aromatic CN heterocycles (Moon et al., 2017; Wu et al., 2020). Taking all together, Cl-doped g-C_3N_4 was successfully synthesized with a nanofibrous structure, and the Cl dopant was covalently introduced to the carbon-nitrogen framework.

3.2. H_2O_2 photosynthesis under the irradiation of various light sources and in the presence and absence of a hole scavenger

The photocatalytic H_2O_2 production on MCC and M under the irradiation of simulated visible sunlight (xenon lamp, $\lambda > 400$ nm) is shown in Fig. 2. In contrast to the negligible amount of H_2O_2 produced on M, MCC catalyzed H_2O_2 generation from water and air to a notable concentration (up to ca. 650 μM) in 6 h, with an average production rate of 1.19 ± 0.06 μM min^{-1}. The H_2O_2 production rate was comparable with other g-C_3N_4-based photocatalysts (Table S3). H_2O_2 was produced via photocatalytic oxygen reduction ($O_2 + 2e^- + 2\,H^+ \rightarrow H_2O_2$) rather than water oxidation ($2\,H_2O \rightarrow H_2O_2 + 2\,H^+ + 2e^-$), as confirmed by the lack of H_2O_2 formation under N_2-saturated condition or in the dark (Fig. 2b). Furthermore, MCC catalyzed the generation of H_2O_2 under various light resources, including white LEDs, visible light (xenon lamp, $\lambda >400$ nm) simulated sunlight (xenon lamp, AM 1.5 G), and outdoor sunlight. As shown in Fig. 3, the H_2O_2 generation rate increased from 0.61 ± 0.05 μM min^{-1} (1.45 ± 0.12 μmol h^{-1}) under white LEDs irradiation to 1.19 ± 0.06 μM min^{-1} (2.86 ± 0.14 μmol h^{-1}) under visible light

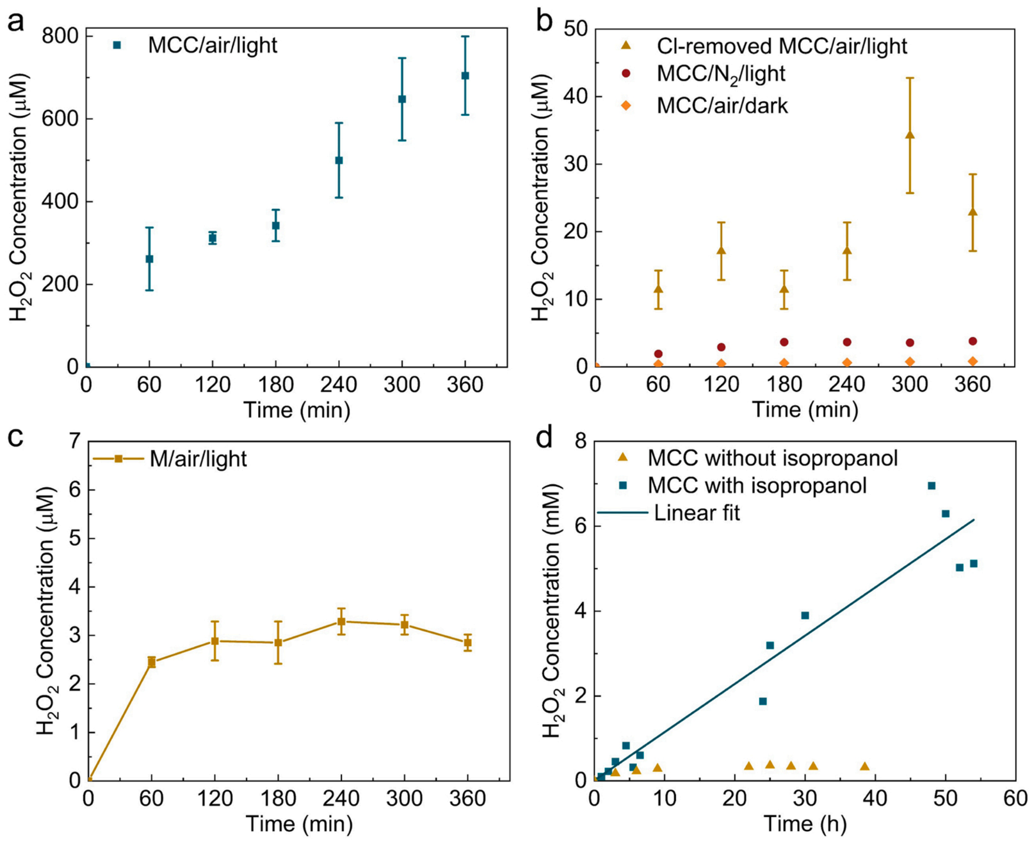

Fig. 2. Photocatalytic H_2O_2 production catalyzed by (a-b) MCC and Cl-removed MCC and (c) M. Experimental conditions were as follows: catalyst load of 1 g L^{-1}, air (1 atm) or N_2 (1 atm), visible light irradiation (xenon lamp, $\lambda > 400$ nm) or in the dark, and 1 mM phosphate buffer (pH 7). (d) Long-term photocatalytic H_2O_2 production catalyzed by MCC with or without the hole scavenger of isopropanol. Experimental conditions were as follows: catalyst load of 1 g L^{-1}, air (1 atm), visible light irradiation (xenon lamp, $\lambda > 400$ nm), and 1 mM phosphate buffer (pH 7) or 1 mM phosphate buffer (pH 7) plus 10% (v/v) isopropanol. Error bars represent the standard deviation.

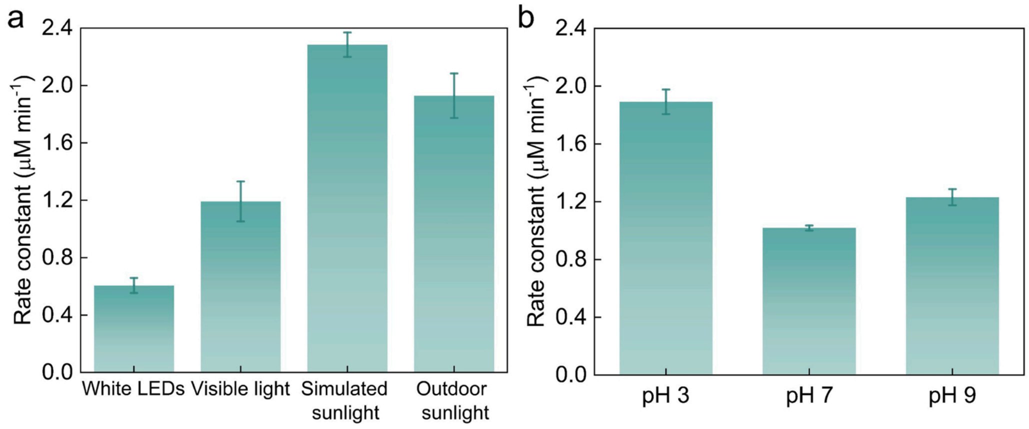

Fig. 3. Photocatalytic H_2O_2 production rate over MCC under various (a) light sources and (b) pH conditions. Experimental conditions for (a) were as follows: catalyst load of 1 g L^{-1}, air (1 atm), irradiation of white LEDs, visible light (xenon lamp, $\lambda > 400$ nm), simulated sunlight (xenon lamp, AM 1.5G), or outdoor sunlight, and 1 mM phosphate buffer (pH 7). Experimental conditions for (b) were as follows: catalyst load of 1 g L^{-1}, air (1 atm), visible light irradiation (xenon lamp, $\lambda > 400$ nm), and 10 mM phosphate or borate buffer (pH 3, 7, or 9). Error bars represent the standard deviation.

irradiation with the increase of irradiance from 10.5 mW cm^{-2} of white LEDs to 12.8 mW cm^{-2} of visible light. Under simulated sunlight irradiation, the H_2O_2 generation rate was further increased to 2.28 ± 0.09 μM min^{-1} (5.47 ± 0.22 μmol h^{-1}) and the SCC was 0.112%, although the irradiance difference between simulated sunlight (12.9 mW cm^{-2}) and visible light was negligible. Meanwhile, the irradiance of outdoor sunlight was the highest (31.2 mW cm^{-2}), but the H_2O_2 generation rate decreased to 1.93 ± 0.16 μM min^{-1} (4.63 ± 0.38 μmol h^{-1}) and the SCC was significantly decreased to 0.0384%. These inconsistencies were induced by the different spectra of diverse light sources (Zheng et al., 2016). Even though the bandgap of MCC is around 1.6 eV (Fig. S5) and the optical absorption of MCC is up to 775 nm, the long-wavelength photons may not be efficiently utilized.

Most previous studies only focused on short-term H_2O_2 production via photocatalysis, i.e., up to several hours, while long-term H_2O_2 generation was largely underexplored. In our study, we evaluated H_2O_2 production under 54 h continuous irradiation of visible sunlight (xenon lamp, $\lambda > 400$ nm). In the system with water and air, substantial net production of H_2O_2 was only observed in the first 6 h of irradiation (Fig. 2d). After that, the accumulated H_2O_2 concentration reached a plateau of 0.33 mM in 20 h. The conduction band energy level of MCC was quantified with Mott-Schottky analysis (Fig. S6) and the valence band edge (VBE) was determined in combination with bandgap analysis (Text S1). The VBE of MCC was less positive than the reduction potential of O_2/H_2O (0.829 versus 1.23 V with respect to NHE, Fig. S7). Hence water oxidation was not thermodynamically feasible. Surprisingly, we did not observe the loss of covalently bonded C-Cl (Fig. S3 and Table S2) or the reduction of charge transfer rate after the 6 h reaction (Fig. S8). MCC did not generate hydroxyl radical, the most powerful oxidant in water, but it produced singlet oxygen with a steady-state concentration of 1.02×10^{-12} M (Text S2), suggesting that one-electron reduction of H_2O_2 to hydroxyl radicals was inhibited and hydroxyl radical was not responsible for destructing or decomposing the photocatalyst. These seemingly contradictory results indicate that photocorrosion induced by holes could occur at the defect sites of the photocatalyst but it did not decompose C-Cl, the key structure for promoting H_2O_2 production (details in Section 3.4). The fact that H_2O_2 production leveled off after the 6 h reaction could also be explained by the comparable decomposition and generation rate of H_2O_2 in the phosphate buffer after H_2O_2 accumulation to a certain level (Shanley, 1953; Knotter et al., 1999). We next introduced 10% (v/v) isopropanol as the hole scavenger for photocatalysis. The oxidation potential of isopropanol is 0.105 V (Al-Azri et al., 2015), less positive than the valence band of MCC (Fig. S7), indicating that scavenging photoinduced holes by isopropanol is thermodynamically favorable. The H_2O_2 production rate was not only improved but also maintained at 2.78 ± 0.10 μM min^{-1} (6.67 ± 0.24 μmol h^{-1}) throughout 54 h (Fig. 2d), realizing continuous accumulation of H_2O_2. The timely quenching of photoinduced holes not only suppressed the recombination of electron-hole pairs but also protected H_2O_2 from further oxidation (Dotan et al., 2011; Hirakawa and Nosaka, 2002; Liu et al., 2015). As a result, H_2O_2 generation was promoted while its decomposition might be inhibited (Hirakawa and Nosaka, 2002; Shi et al., 2017), leading to substantial net production of H_2O_2.

3.3. *Acidic condition promoting H_2O_2 photosynthesis*

As shown in Fig. 3b, with the decrease of pH from 7 to 3, the H_2O_2 generation rate increased from 1.02 ± 0.02 μM min^{-1} to 1.89 ± 0.09 μM min^{-1}. On the contrary, increasing the pH from 7 to 9 did not have a statistically significant influence on the H_2O_2 generation rate (i.e., 1.02 ± 0.02 versus 1.26 ± 0.22 μM min^{-1} at pH 7 and pH 9, respectively). The higher concentration of protons at the lower pH was believed to accelerate the protonation of adsorbed O_2, however, the proton concentration was too low at both pH 7 and pH 9 to enhance the rate of H_2O_2 production. According to molecular simulation (Fig. 4), the pKa of Cl-doped moiety was predicted to be 4.7 (pKa_1) and 2.7 (pKa_2), respectively. In contrast, the pKa_1 and pKa_2 of the hydrogenated derivative without the presence of Cl dopants were 7.6 and 2.8, respectively. The calculated range of pKa_s between 3 and 8 is consistent with that for the greatest variation of the H_2O_2 production rate as observed in our experiments (Fig. 3). When the pH value of the reaction system was 3, some of the chlorinated moieties and their hydrogenated derivatives were doubly protonated. To further understand the faster H_2O_2 generation rate at acidic conditions, the O_2 binding affinity onto a g-C_3N_4 substrate was calculated by the following equation:

$$E_{binding} = E_{GCN} + E_{O_2} - E_{GCN/O_2} \qquad (4)$$

Where E_{GCN}, E_{O_2}, and E_{GCN/O_2} refer to the energy of the g-C_3N_4 substrate, O_2, and g-C_3N_4/O_2 adduct, respectively. For the singly protonated Cl-doped g-C_3N_4 and its hydrogenated derivative without Cl (Fig. 5a and 5b), their $E_{binding}$s were – 72.0 and – 80.5 kcal mol^{-1}, respectively. In contrast, the doubly protonated moieties (Figs. 5c and 5d) afforded remarkably positive $E_{binding}$s of 56.0 and 62.5 kcal mol^{-1}, suggesting enhanced O_2 binding and faster H_2O_2 production at a lower pH. The bound O_2 was probably first protonated before grabbing an electron transferred from the g-C_3N_4 to trigger its desorption. One should note that the slightly stronger binding with O_2 over the doubly protonated hydrogenated g-C_3N_4 (62.5 kcal mol^{-1}, Fig. 5b) does not necessarily mean a higher efficiency on H_2O_2 production since over-binding could impede product desorption. In addition, other factors including, reaction temperature, the presence of UV irradiation, and the mass transfer rate in the reaction system, could also play an important role in determining the performance of H_2O_2 photosynthesis.

3.4. *Cl dopant being critical to enhanced H_2O_2 photosynthesis*

Post-thermal treatment in a controlled atmosphere is an effective method for removing impurity elements while maintaining the morphology, crystal structure, and vibrational modes of g-C_3N_4 (Dillip et al., 2017; Xie et al., 2016). To further investigate the role of the Cl dopant in the H_2O_2 photosynthesis on MCC, we intentionally created a Cl-removed g-C_3N_4 sample. Both XPS analysis (Fig. S3) and EDS mapping (Fig. 6) confirmed that post-thermal treatment successfully removed the Cl element from MCC, but the morphology of the photocatalyst remained (Figs. 6a and 6b). Compared with MCC, the FTIR spectrum of the Cl-removed g-C_3N_4 did not show a significant difference, while the atomic ratio of carbon to nitrogen was increased from 1.08 to 1.22 and the atomic percentage of oxygen decreased from 11.7% to 2.3%. To exam the influence of oxygen, we tested the H_2O_2 production efficiency of pristine and oxidized g-C_3N_4 nanosheets. The oxidized g-C_3N_4 sample was produced by photocatalytic ozonation as reported in our previous work, which has confirmed to exclusively introduce oxygen dopants into the carbon-nitrogen framework (Li et al., 2021). As shown in Fig. S9, the improvement of the H_2O_2 generation rate was negligible although the atomic percentage of oxygen was increased from 1.0% to 7.8%. On the contrary, H_2O_2 production was largely inhibited after removing the Cl dopant (Fig. 2b), with the generation rate decreasing from 1.19 ± 0.06 μM min^{-1} to 0.06 ± 0.07 μM min^{-1}. Taken all together, Cl dopants are indispensable for H_2O_2 production.

What is more, the presence of Cl dopants modified the bandgap of g-C_3N_4 even though the atomic percentage of the covalently bonded Cl was as low as ~1.2% (Table S2). As shown in Fig. S5, in contrast to sample M (Zheng et al., 2016), both MCC and Cl-removed MCC could absorb visible light photons, with bandgaps of 1.60 and 1.07 eV, respectively. As a result, MCC and Cl-removed MCC could absorb a wider spectrum of photons and produce more photoinduced charge

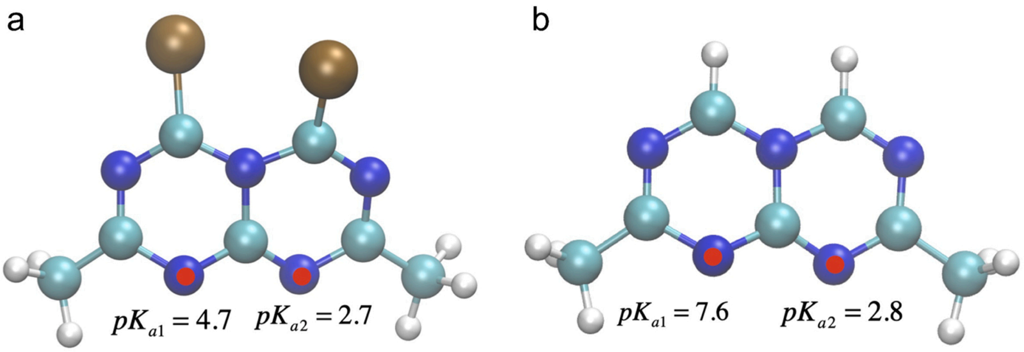

Fig. 4. Predicted pKa values for (a) the Cl-doped moiety and (b) its hydrogenated derivatives (also known as Cl-removed derivatives). The nitrogen, carbon, chlorine, and hydrogen atoms are colored blue, cyan, brown, and white, respectively.

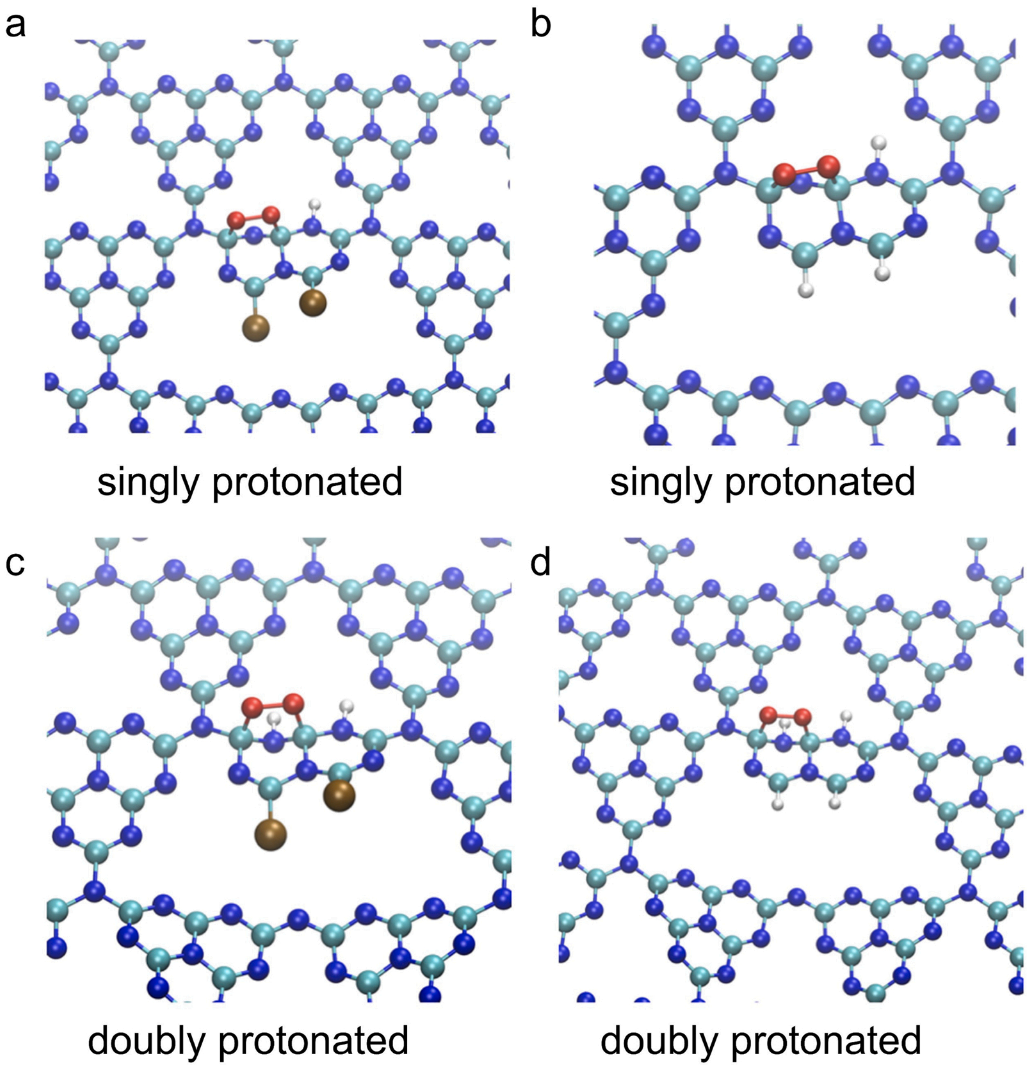

Fig. 5. Optimized O_2 binding structures on (a) singly protonated Cl-doped g-C_3N_4, (b) singly protonated hydrogenated g-C_3N_4, (c) doubly protonated Cl-doped g-C_3N_4, and (d) doubly protonated hydrogenated g-C_3N_4. The hydrogenated g-C_3N_4 is equivalent to Cl-removed g-C_3N_4 in our study. The nitrogen, carbon, oxygen, chlorine, and hydrogen atoms are colored blue, cyan, red, brown, and white, respectively.

carriers than M. In addition, the thermal treatment process not only removed the covalently bonded Cl atoms but also decreased the atomic percentage of O from 11.7% to 2.3% (Table S2), together with a possible change of C and N contents, which may explain the smaller bandgap of Cl-removed MCC. The effect of Cl dopants on the interfacial charge transfer of g-C_3N_4 was evaluated by the EIS. As shown in Fig. S8, MCC exhibited the smallest semicircle thus it possessed the lowest charge-transfer resistance (Wei et al., 2018b; Xi et al., 2019; Xu et al., 2020; Zhao et al., 2014). However, when the covalently bonded Cl was removed through annealing, the charge-transfer resistance increased significantly, possibly inhibiting H_2O_2 production.

A two-step reaction pathway for g-C_3N_4-catalyzed H_2O_2 production is proposed as shown in Fig. 7. Specifically, the first step is the breaking of a C-O bond upon single protonation of O_2, while the second step is the breaking of another C-O bond that leads to the desorption of the produced H_2O_2 from the g-C_3N_4 substrate upon further protonation. For each of these two steps, its reaction energy, ΔG, and activation energy, ΔG^{act}, can be calculated by

$$\Delta G = E_{product} - E_{reactant} - E_{H^+} \quad (5)$$

and

$$\Delta G^{act} = E_{transition} - E_{reactant} - E_{H^+} \quad (6)$$

respectively, where $E_{reactant}$, $E_{transition}$, $E_{product}$, and E_{H^+} are the energy of the reactant, transition state, product, and solvated proton, respectively. A value of $-$ 262.23 kcal mol^{-1} was adopted for E_{H^+} as suggested by a study of protonated water clusters embedded in a dielectric medium (Tawa et al., 1998). Moreover, the DIMER method (Henkelman and Jónsson, 1999) was utilized to locate the transition state between a given pair of reactants and products by minimizing the curvature mode of the potential energy surface. It was found that $\Delta G_1 = -12.9\ kcal\ mol^{-1}$ and $\Delta G_1{}^{act} = 4.4\ kcal\ mol^{-1}$ for the Cl-doped g-C_3N_4, while their counter parts for the Cl-removed g-C_3N_4 are $\Delta G_1 = -13.8\ kcal\ mol^{-1}$ and $\Delta G_1{}^{act} = 4.6\ kcal\ mol^{-1}$, respectively. In contrast to the similarity in the energy of the first step between the Cl-doped g-C_3N_4 and its Cl-removed derivative, they have distinct activation energies for the second step. For the Cl-doped g-C_3N_4, $\Delta G_2{}^{act} = 27.0\ kcal\ mol^{-1}$, which is much lower than $\Delta G_2{}^{act} = 33.2\ kcal\ mol^{-1}$ for the Cl-removed g-C_3N_4. Since $\Delta G_2{}^{act}$ is substantially higher than $\Delta G_1{}^{act}$, the second step was ascertained as the time-limiting step for H_2O_2 production. As a result, the difference in $\Delta G_2{}^{act}$ by ~6 kcal mol^{-1} and thus a huge difference in the resultant charge transfer rate (Fig. S8) could lead to a significantly faster H_2O_2 production over the Cl-doped g-C_3N_4.

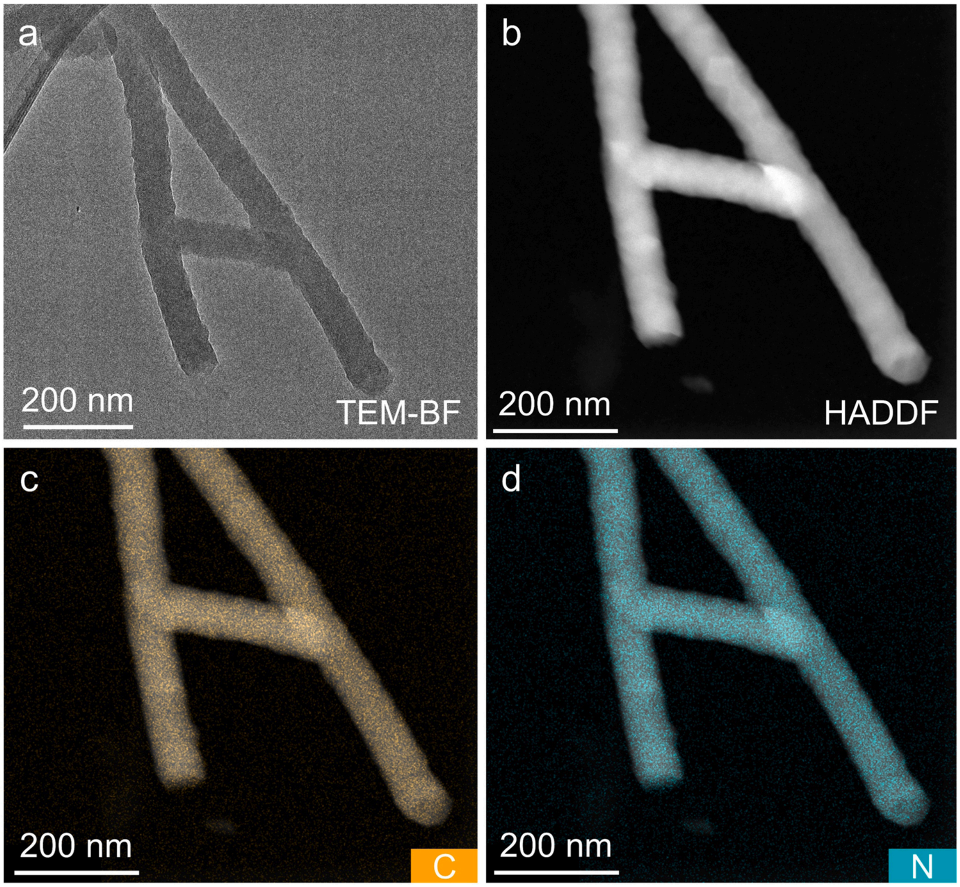

Fig. 6. (a) Bright-field (BF) transmission electron microscopy (TEM), (b) high-angle annular dark-field scanning transmission electron microscopy (HAADF-STEM), and energy dispersive X-ray spectroscopy (EDS) mapping of (c) C and (d) N of annealed Cl-doped graphitic carbon nitride. Cl was not detected.

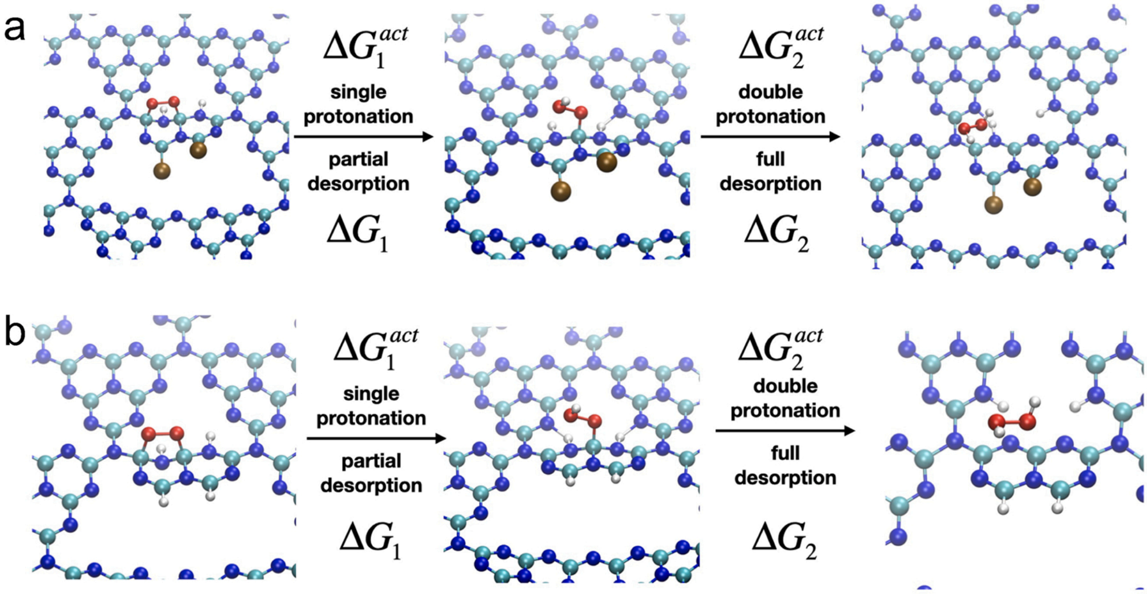

Fig. 7. Proposed reaction pathways for H_2O_2 production catalyzed by (a) Cl-doped g-C_3N_4 and (b) its Cl-removed derivative. The nitrogen, carbon, oxygen, chlorine, and hydrogen atoms are colored blue, cyan, red, brown, and white, respectively.

4. Conclusions and implications

In conclusion, Cl-doped g-C_3N_4 was successfully synthesized via a facile method for producing H_2O_2 efficiently. Under visible light irradiation, Cl-doped g-C_3N_4 displayed noteworthy photocatalytic performance by building up a cumulative H_2O_2 concentration to 650 μM in 6 h without an organic scavenger. In contrast, only 2–5 μM of H_2O_2 was produced over the undoped g-C_3N_4 under the same experimental conditions. Furthermore, the presence of isopropanol as the hole scavenger enhanced the rate of H_2O_2 generation by 2.3-fold, and H_2O_2 was continuously produced for up to 54 h without leveling off. The immediate consumption of holes by the scavenger promoted the separation of photoinduced electron-hole pairs, protected produced H_2O_2 from decomposition, and prevented the photocatalyst from photocorrosion. The adsorbed O_2 over the g-C_3N_4 surface is reduced via two steps of protonation for producing H_2O_2, and the second protonation step is the rate-determining one. With an integrated approach of molecular simulations and microscopic and spectroscopic characterizations, the critical role of Cl dopants in promoting H_2O_2 photosynthesis has been identified. The Cl dopant improved the charge transfer rate, reduced the bandgap of g-C_3N_4, and lowered the activation energy of the rate-limiting step of O_2 protonation.

H_2O_2 is one of the most common disinfectants and it shows broad-spectrum antimicrobial activities against environmental pathogens. It is also effective for removing hydrogen sulfide, reduced iron, reduced manganese, etc. from water reservoirs and for water reuse. However, the large-scale production of H_2O_2 relies on the anthraquinone process and involves the utilization of hazardous materials and chemicals. Our work realizes continuous solar-driven photocatalytic generation of H_2O_2 with chlorine-doped g-C_3N_4. This green and sustainable process is not only promising in supplementing or partially alternating the centralized industrial process but also can be easily incorporated into small-scale disinfection units. In developed countries, solar-driven photocatalytic production of H_2O_2 exhibits broad applicability in the urban rooftop design, where the collected rainwater can be disinfected for plant irradiation, building cleaning, toilet flushing, and pond refilling. In developing countries and rural communities, solar-driven photocatalysis is an economical and technologically feasible method to produce H_2O_2 without the need for large infrastructures, expensive instruments, toxic reagents, or high professional personnel. Our work not only provides guidelines for advancing photocatalysis with non-metal doping but also sheds light on the sustainable production of H_2O_2 for practical engineering applications.

Environmental Implications

H_2O_2 is among the most common disinfectants showing broad-spectrum inactivating efficacy against viruses, bacteria, bacterial spores, and fungi. It is also effective in removing hydrogen sulfide, iron, manganese, etc. from reused water and water reservoirs. However, the large-scale production of H_2O_2 relies on the anthraquinone process and involves the utilization of hazardous materials. Our work realizes continuous solar-driven photocatalytic generation of H_2O_2 with chlorine-doped g-C_3N_4, which is promising in supplementing or partially alternating the centralized industrial process. This work not only provides guidelines for advancing photocatalysis with non-metal doping but also sheds light on the sustainable production of H_2O_2.

CRediT authorship contribution statement

Mengqiao Li: Investigation, Formal analysis, Data curation, Writing – original draft, Writing – review & editing. **Qinmin Zheng:** Conceptualization, Investigation, Methodology, Formal analysis, Data curation. **David P. Durkin:** Resources, Formal analysis, Data curation, Validation. **Hanning Chen:** Formal analysis, Data curation, Validation, Software, Visualization, Writing – review & editing. **Danmeng Shuai:** Supervision, Funding acquisition, Writing – review & editing.

Declaration of Competing Interest

The authors declare that they have no known competing financial interests or personal relationships that could have appeared to influence the work reported in this paper.

Acknowledgment

We acknowledge NSF Grants CHE-1807617 for supporting our study. We also acknowledge the Air Force Office of Scientific Research (MIPR# F4FGA08354G001) and the United States Naval Academy for facilities support. Computational resources were provided by the Argonne Leadership Computing Facilities at Argonne National Laboratory under Department of Energy contract DE-AC-06CH11357 and by the Extreme Science and Engineering Discovery Environment at Texas Advanced Computing Center under National Science Foundation contract TG-CHE130008. We thank Dr. Julio A. N. T. Soares at the University of Illinois at Urbana-Champaign for the bandgap analysis.

Appendix A. Supporting information

Supplementary data associated with this article can be found in the online version at doi:10.1016/j.jhazmat.2022.129251.

References

Al-Azri, Z.H.N., Chen, W.-T., Chan, A., Jovic, V., Ina, T., Idriss, H., Waterhouse, G.I.N., 2015. The roles of metal co-catalysts and reaction media in photocatalytic hydrogen production: Performance evaluation of M/TiO_2 photocatalysts (M = Pd, Pt, Au) in different alcohol–water mixtures. J. Catal. 329, 355–367. https://doi.org/10.1016/j.jcat.2015.06.005.

Bader, H., Sturzenegger, V., Hoigné, J., 1988. Photometric method for the determination of low concentrations of hydrogen peroxide by the peroxidase catalyzed oxidation of N,N-diethyl-p-phenylenediamine (DPD). Water Res 22, 1109–1115. https://doi.org/10.1016/0043-1354(88)90005-X.

Bani-Hashemian, M.H., Brück, S., Luisier, M., VandeVondele, J., 2016. A generalized Poisson solver for first-principles device simulations. J. Chem. Phys. 144, 044113 https://doi.org/10.1063/1.4940796.

Baran, T., Wojtyła, S., Minguzzi, A., Rondinini, S., Vertova, A., 2019. Achieving efficient H_2O_2 production by a visible-light absorbing, highly stable photosensitized TiO_2. Appl. Catal. B 244, 303–312. https://doi.org/10.1016/j.apcatb.2018.11.044.

Campos-Martin, J.M., Blanco-Brieva, G., Fierro, J.L.G., 2006. Hydrogen peroxide synthesis: an outlook beyond the anthraquinone process. Angew. Chem. Int. Ed. 45, 6962–6984. https://doi.org/10.1002/anie.200503779.

Csizmadia, F., Tsantili-Kakoulidou, A., Panderi, I., Darvas, F., 1997. Prediction of distribution coefficient from structure. 1. estimation method. J. Pharm. Sci. 86, 865–871. https://doi.org/10.1021/js960177k.

Cui, Y., Ding, Z., Fu, X., Wang, X., 2012. Construction of conjugated carbon nitride nanoarchitectures in solution at low temperatures for photoredox catalysis. Angew. Chem. Int. Ed. 51, 11814–11818. https://doi.org/10.1002/anie.201206534.

Dillip, G.R., Sreekanth, T.V.M., Joo, S.W., 2017. Tailoring the bandgap of N-rich graphitic carbon nitride for enhanced photocatalytic activity. Ceram. Int. 43, 6437–6445. https://doi.org/10.1016/j.ceramint.2017.02.057.

Dotan, H., Sivula, K., Grätzel, M., Rothschild, A., Warren, S.C., 2011. Probing the photoelectrochemical properties of hematite (α-Fe_2O_3) electrodes using hydrogen peroxide as a hole scavenger. Energy Environ. Sci. 4, 958–964. https://doi.org/10.1039/C0EE00570C.

Fukuzumi, S., Lee, Y.-M., Nam, W., 2018. Solar-driven production of hydrogen peroxide from water and dioxygen. Chem.: Eur. J. 24, 5016–5031. https://doi.org/10.1002/chem.201704512.

Goedecker, S., Teter, M., Hutter, J., 1996. Separable dual-space Gaussian pseudopotentials. Phys. Rev. B 54, 1703–1710. https://doi.org/10.1103/PhysRevB.54.1703.

Goldstein, S., Aschengrau, D., Diamant, Y., Rabani, J., 2007. Photolysis of aqueous H_2O_2: quantum yield and applications for polychromatic uv actinometry in photoreactors. Environ. Sci. Technol. 41, 7486–7490. https://doi.org/10.1021/es071379t.

Goliaei, E.M., Seriani, N., 2019. Structure and electronic properties of small silver–gold clusters on titania photocatalysts for H_2O_2 production: an investigation with density functional theory. J. Phys. Chem. C. 123, 2855–2863. https://doi.org/10.1021/acs.jpcc.8b09300.

Grand View Research, 2021. Hydrogen Peroxide Market Size, Share & Trends Analysis Report By Function (Oxidant, Disinfectant, Bleaching), By Application (Healthcare, Wastewater Treatment), By Region, And Segment Forecasts, 2021 - 2028 (Industry analysis No. GVR-4–68038-783–4).

Gu, Q., Gao, Z., Xue, C., 2016. Self-sensitized carbon nitride microspheres for long-lasting visible-light-driven hydrogen generation. Small 12, 3543–3549. https://doi.org/10.1002/smll.201600181.

Guo, F., Li, M., Ren, H., Huang, X., Shu, K., Shi, W., Lu, C., 2019. Facile bottom-up preparation of Cl-doped porous g-C_3N_4 nanosheets for enhanced photocatalytic degradation of tetracycline under visible light. Sep. Purif. Technol. 228, 115770 https://doi.org/10.1016/j.seppur.2019.115770.

Han, E.-X., Li, Y.-Y., Wang, Q.-H., Huang, W.-Q., Luo, L., Hu, W., Huang, G.-F., 2019. Chlorine doped graphitic carbon nitride nanorings as an efficient photoresponsive catalyst for water oxidation and organic decomposition. J. Mater. Sci. Technol. 35, 2288–2296. https://doi.org/10.1016/j.jmst.2019.05.057.

Henkelman, G., Jónsson, H., 1999. A dimer method for finding saddle points on high dimensional potential surfaces using only first derivatives. J. Chem. Phys. 111, 7010–7022. https://doi.org/10.1063/1.480097.

Hirakawa, H., Shiota, S., Shiraishi, Y., Sakamoto, H., Ichikawa, S., Hirai, T., 2016. Au nanoparticles supported on $BiVO_4$: effective inorganic photocatalysts for H_2O_2 production from water and O_2 under Visible Light. ACS Catal. 6, 4976–4982. https://doi.org/10.1021/acscatal.6b01187.

Hirakawa, T., Nosaka, Y., 2002. Properties of $O_2^{\bullet-}$ and $OH^{\bullet}$ formed in TiO_2 aqueous suspensions by photocatalytic reaction and the influence of H_2O_2 and some ions. Langmuir 18, 3247–3254. https://doi.org/10.1021/la015685a.

Hohenberg, P., Kohn, W., 1964. Inhomogeneous electron gas. Phys. Rev. 136, B864–B871. https://doi.org/10.1103/PhysRev.136.B864.

Kim, H., Kwon, O.S., Kim, S., Choi, W., Kim, J.-H., 2016. Harnessing low energy photons (635 nm) for the production of H_2O_2 using upconversion nanohybrid photocatalysts. Energy Environ. Sci. 9, 1063–1073. https://doi.org/10.1039/C5EE03115J.

Kim, K., Park, J., Kim, H., Jung, G.Y., Kim, M.-G., 2019. Solid-phase photocatalysts: physical vapor deposition of Au nanoislands on porous TiO_2 films for millimolar H_2O_2 production within a few minutes. ACS Catal. 9, 9206–9211. https://doi.org/10.1021/acscatal.9b02269.

Knotter, D.M., de Gendt, S., Baeyens, M., Mertens, P.W., Heyns, M.M., 1999. Hydrogen peroxide decomposition in ammonia solutions. J. Electrochem. Soc. 146, 3476–3481. https://doi.org/10.1149/1.1392499.

Krukau, A.V., Vydrov, O.A., Izmaylov, A.F., Scuseria, G.E., 2006. Influence of the exchange screening parameter on the performance of screened hybrid functionals. J. Chem. Phys. 125, 224106 https://doi.org/10.1063/1.2404663.

Li, C., Yu, S., Zhang, X., Wang, Y., Liu, C., Chen, G., Dong, H., 2019. Insight into photocatalytic activity, universality and mechanism of copper/chlorine surface dual-doped graphitic carbon nitride for degrading various organic pollutants in water. J. Colloid Interface Sci. 538, 462–473. https://doi.org/10.1016/j.jcis.2018.12.009.

Li, H., Shan, C., Pan, B., 2018. Fe(III)-doped g-C_3N_4 mediated peroxymonosulfate activation for selective degradation of phenolic compounds via high-valent iron-oxo species. Environ. Sci. Technol. 52, 2197–2205. https://doi.org/10.1021/acs.est.7b05563.

Li, M., Liu, D., Chen, X., Yin, Z., Shen, H., Aiello, A., McKenzie, K.R., Jiang, N., Li, X., Wagner, M.J., Durkin, D.P., Chen, H., Shuai, D., 2021. Radical-Driven Decomposition of Graphitic Carbon Nitride Nanosheets: Light Exposure Matters. Environ. Sci. Technol. 55, 12414–12423. https://doi.org/10.1021/acs.est.1c03804.

Li, S., Dong, G., Hailili, R., Yang, L., Li, Y., Wang, F., Zeng, Y., Wang, C., 2016. Effective photocatalytic H_2O_2 production under visible light irradiation at g-C_3N_4 modulated by carbon vacancies. Appl. Catal. B 190, 26–35. https://doi.org/10.1016/j.apcatb.2016.03.004.

Liang, Q., Li, Z., Huang, Z.-H., Kang, F., Yang, Q.-H., 2015. Holey Graphitic Carbon Nitride Nanosheets with Carbon Vacancies for Highly Improved Photocatalytic Hydrogen Production. Adv. Funct. Mater. 25, 6885–6892. https://doi.org/10.1002/adfm.201503221.

Liu, J., Wang, H., Antonietti, M., 2016. Graphitic carbon nitride "reloaded": emerging applications beyond (photo)catalysis. Chem. Soc. Rev. 45, 2308–2326. https://doi.org/10.1039/C5CS00767D.

Liu, J., Liu, Y., Liu, N., Han, Y., Zhang, X., Huang, H., Lifshitz, Y., Lee, S.-T., Zhong, J., Kang, Z., 2015. Metal-free efficient photocatalyst for stable visible water splitting via a two-electron pathway. Science 347, 970–974. https://doi.org/10.1126/science.aaa3145.

Long, D., Diao, W., Rao, X., Zhang, Y., 2020. Boosting the photocatalytic hydrogen evolution performance of Mg- and Cl-doped graphitic carbon nitride microtubes. ACS Appl. Energy Mater. 3, 9278–9284. https://doi.org/10.1021/acsaem.0c01619.

Melchionna, M., Fornasiero, P., Prato, M., 2019. The rise of hydrogen peroxide as the main product by metal-free catalysis in oxygen reductions. Adv. Mater. 31, 1802920. https://doi.org/10.1002/adma.201802920.

Moon, G., Fujitsuka, M., Kim, S., Majima, T., Wang, X., Choi, W., 2017. Eco-friendly photochemical production of H_2O_2 through O_2 reduction over carbon nitride frameworks incorporated with multiple heteroelements. ACS Catal. 7, 2886–2895. https://doi.org/10.1021/acscatal.6b03334.

Myers, R.L., 2007. The 100 most important chemical compounds: a reference guide. Greenwood Press, Westport, Conn.

Nosaka, Y., Y. Nosaka, A., 2017. Generation and detection of reactive oxygen species in photocatalysis. Chem. Rev. 117, 11302–11336. https://doi.org/10.1021/acs.chemrev.7b00161.

Ong, W.-J., Tan, L.-L., Ng, Y.H., Yong, S.-T., Chai, S.-P., 2016. Graphitic carbon nitride (g-C_3N_4)-based photocatalysts for artificial photosynthesis and environmental remediation: are we a step closer to achieving sustainability? Chem. Rev. 116, 7159–7329. https://doi.org/10.1021/acs.chemrev.6b00075.

Shanley, E.S., 1953. Self-heating of hydrogen peroxide storage vessels. Ind. Eng. Chem. 45, 1520–1524. https://doi.org/10.1021/ie50523a044.

Shen, H., Durkin, D.P., Aiello, A., Diba, T., Lafleur, J., Zara, J.M., Shen, Y., Shuai, D., 2021. Photocatalytic graphitic carbon nitride-chitosan composites for pathogenic biofilm control under visible light irradiation. J. Hazard. Mater. 408, 124890 https://doi.org/10.1016/j.jhazmat.2020.124890.

Shi, L., Yang, L., Zhou, W., Liu, Y., Yin, L., Hai, X., Song, H., Ye, J., 2018. Photoassisted construction of holey defective g-C_3N_4 photocatalysts for efficient visible-light-driven H_2O_2 production. Small 14, 1703142. https://doi.org/10.1002/smll.201703142.

Shi, X., Siahrostami, S., Li, G.-L., Zhang, Y., Chakthranont, P., Studt, F., Jaramillo, T.F., Zheng, X., Nørskov, J.K., 2017. Understanding activity trends in electrochemical water oxidation to form hydrogen peroxide. Nat. Commun. 8, 701. https://doi.org/10.1038/s41467-017-00585-6.

Shiraishi, Y., Kanazawa, S., Tsukamoto, D., Shiro, A., Sugano, Y., Hirai, T., 2013. Selective hydrogen peroxide formation by titanium dioxide photocatalysis with benzylic alcohols and molecular oxygen in water. ACS Catal. 3, 2222–2227. https://doi.org/10.1021/cs400511q.

Shiraishi, Y., Kanazawa, S., Kofuji, Y., Sakamoto, H., Ichikawa, S., Tanaka, S., Hirai, T., 2014a. Sunlight-driven hydrogen peroxide production from water and molecular oxygen by metal-free photocatalysts. Angew. Chem. Int. Ed. 53, 13454–13459. https://doi.org/10.1002/anie.201407938.

Shiraishi, Y., Kanazawa, S., Sugano, Y., Tsukamoto, D., Sakamoto, H., Ichikawa, S., Hirai, T., 2014b. Highly selective production of hydrogen peroxide on graphitic carbon nitride (g-C_3N_4) photocatalyst activated by visible light. ACS Catal. 4, 774–780. https://doi.org/10.1021/cs401208c.

Su, F., Mathew, S.C., Lipner, G., Fu, X., Antonietti, M., Blechert, S., Wang, X., 2010. mpg-C_3N_4-catalyzed selective oxidation of alcohols using O_2 and visible light. J. Am. Chem. Soc. 132, 16299–16301. https://doi.org/10.1021/ja102866p.

Tauc, J., Grigorovici, R., Vancu, A., 1966. Optical properties and electronic structure of amorphous germanium. Phys. Stat. Sol. (b) 15, 627–637. https://doi.org/10.1002/pssb.19660150224.

Tawa, G.J., Topol, I.A., Burt, S.K., Caldwell, R.A., Rashin, A.A., 1998. Calculation of the aqueous solvation free energy of the proton. J. Chem. Phys. 109, 4852–4863. https://doi.org/10.1063/1.477096.

Teng, Z., Zhang, Q., Yang, H., Kato, K., Yang, W., Lu, Y.-R., Liu, S., Wang, C., Yamakata, A., Su, C., Liu, B., Ohno, T., 2021. Atomically dispersed antimony on carbon nitride for the artificial photosynthesis of hydrogen peroxide. Nat. Catal. 4, 374–384. https://doi.org/10.1038/s41929-021-00605-1.

VandeVondele, J., Krack, M., Mohamed, F., Parrinello, M., Chassaing, T., Hutter, J., 2005. Quickstep: Fast and accurate density functional calculations using a mixed Gaussian and plane waves approach. Comput. Phys. Commun. 167, 103–128. https://doi.org/10.1016/j.cpc.2004.12.014.

Wang, K.-L., Li, Y., Sun, T., Mao, F., Wu, J.-K., Xue, B., 2019. Fabrication of Na, Cl co-doped graphitic carbon nitride with enhanced photocatalytic activity for degradation of dyes and antibiotics. J. Mater. Sci: Mater. Electron 30, 4446–4454. https://doi.org/10.1007/s10854-019-00733-2.

Wang, X., Maeda, K., Thomas, A., Takanabe, K., Xin, G., Carlsson, J.M., Domen, K., Antonietti, M., 2009. A metal-free polymeric photocatalyst for hydrogen production from water under visible light. Nat. Mater. 8, 76–80. https://doi.org/10.1038/nmat2317.

Wei, F., Liu, Y., Zhao, H., Ren, X., Liu, J., Hasan, T., Chen, L., Li, Y., Su, B.-L., 2018b. Oxygen self-doped g-C_3N_4 with tunable electronic band structure for unprecedentedly enhanced photocatalytic performance. Nanoscale 10, 4515–4522. https://doi.org/10.1039/C7NR09660G.

Wei, Z., Liu, M., Zhang, Z., Yao, W., Tan, H., Zhu, Y., 2018a. Efficient visible-light-driven selective oxygen reduction to hydrogen peroxide by oxygen-enriched graphitic carbon nitride polymers. Energy Environ. Sci. 11, 2581–2589. https://doi.org/10.1039/C8EE01316K.

Woon, D.E., Dunning, T.H., 1994. Gaussian basis sets for use in correlated molecular calculations. IV. Calculation of static electrical response properties. J. Chem. Phys. 100, 2975–2988. https://doi.org/10.1063/1.466439.

Wu, S., Yu, H., Chen, S., Quan, X., 2020. Enhanced photocatalytic H_2O_2 production over carbon nitride by doping and defect engineering. ACS Catal. 10, 14380–14389. https://doi.org/10.1021/acscatal.0c03359.

Xi, J., Xia, H., Ning, X., Zhang, Z., Liu, J., Mu, Z., Zhang, S., Du, P., Lu, X., 2019. Carbon-intercalated 0D/2D hybrid of hematite quantum dots/graphitic carbon nitride nanosheets as superior catalyst for advanced oxidation. Small 15, 1902744. https://doi.org/10.1002/smll.201902744.

Xie, X., Fan, X., Huang, X., Wang, T., He, J., 2016. In situ growth of graphitic carbon nitride films on transparent conducting substrates via a solvothermal route for photoelectrochemical performance. RSC Adv. 6, 9916–9922. https://doi.org/10.1039/C5RA21228F.

Xiong, T., Wang, H., Zhou, Y., Sun, Y., Cen, W., Huang, H., Zhang, Y., Dong, F., 2018. KCl-mediated dual electronic channels in layered g-C_3N_4 for enhanced visible light photocatalytic NO removal. Nanoscale 10, 8066–8074. https://doi.org/10.1039/C8NR01433G.

Xu, F., Meng, K., Cheng, B., Wang, S., Xu, J., Yu, J., 2020. Unique S-scheme heterojunctions in self-assembled TiO_2/$CsPbBr_3$ hybrids for CO_2 photoreduction. Nat. Commun. 11, 4613. https://doi.org/10.1038/s41467-020-18350-7.

Yang, Y., Jin, H., Zhang, C., Gan, H., Yi, F., Wang, H., 2020. Nitrogen-deficient modified P–Cl co-doped graphitic carbon nitride with enhanced photocatalytic performance. J. Alloy. Compd. 821, 153439 https://doi.org/10.1016/j.jallcom.2019.153439.

Yi, F., Gan, H., Jin, Hufang, Zhao, W., Zhang, K., Jin, Huixia, Zhang, H., Qian, Y., Ma, J., 2020. Sulfur- and chlorine-co-doped g-C_3N_4 nanosheets with enhanced active species generation for boosting visible-light photodegradation activity. Sep. Purif. Technol. 233, 115997 https://doi.org/10.1016/j.seppur.2019.115997.

Zhao, Huanxin, Quan H., Yu, Chen, X., Zhang, S., Zhao, Y., Wang, H, Huimin, 2014. Fabrication of atomic single layer graphitic-C_3N_4 and its high performance of photocatalytic disinfection under visible light irradiation. Appl. Catal. B 152–153, 46–50. https://doi.org/10.1016/j.apcatb.2014.01.023.

Zheng, Q., Shen, H., Shuai, D., 2017. Emerging investigators series: advances and challenges of graphitic carbon nitride as a visible-light-responsive photocatalyst for sustainable water purification. Environ. Sci.: Water Res. Technol. 3, 982–1001. https://doi.org/10.1039/C7EW00159B.

Zheng, Q., Durkin, D.P., Elenewski, J.E., Sun, Y., Banek, N.A., Hua, L., Chen, H., Wagner, M.J., Zhang, W., Shuai, D., 2016. Visible-light-responsive graphitic carbon nitride: rational design and photocatalytic applications for water treatment. Environ. Sci. Technol. 50, 12938–12948. https://doi.org/10.1021/acs.est.6b02579.

Zhou, Z., Li, M., Kuai, C., Zhang, Y., Smith, V.F., Lin, F., Aiello, A., Durkin, D.P., Chen, H., Shuai, D., 2021. Fe-based single-atom catalysis for oxidizing contaminants of emerging concern by activating peroxides. J. Hazard. Mater. 418, 126294 https://doi.org/10.1016/j.jhazmat.2021.126294.

Zhu, Q., Xu, Z., Qiu, B., Xing, M., Zhang, J., 2021. Emerging Cocatalysts on g-C_3N_4 for Photocatalytic Hydrogen Evolution. Small 17, 2101070. https://doi.org/10.1002/smll.202101070.

Zhu, Q., Qiu, B., Du, M., Ji, J., Nasir, M., Xing, M., Zhang, J., 2020. Dopant-induced edge and basal plane catalytic sites on ultrathin c3n4 nanosheets for photocatalytic water reduction. ACS Sustain. Chem. Eng. 8, 7497–7502. https://doi.org/10.1021/acssuschemeng.0c02122.